Product-state control through interfering two-photon ionization routes

Feng Wang[1,*] and D. S. Elliott[2]
[1]Department of Physics and School of Electrical and Computer Engineering, Purdue University, West Lafayette, Indiana 47907
[2]School of Electrical and Computer Engineering, Purdue University, West Lafayette, Indiana 47907
(Received 21 January 1997)

We have extended our studies of control of the branching ratio for photoionization of atomic barium. This control is based on an interference between two distinct photoexcitation routes, each of which is a resonantly enhanced two-photon process. We report our experimental studies of the dependence of the interference on atomic beam density, laser power, selection of intermediate states, and relative polarization of the two field components. We observe that the potential for product control increases dramatically with increasing atomic beam density and depends strongly on the laser pulse energies as well. [S1050-2947(97)01410-8]

PACS number(s): 32.80.Qk, 32.80.Fb

I. INTRODUCTION

The exploitation of the interference between optical excitation pathways as a means of controlling branching ratios for photofragmentation processes [1] has been advanced by several recent experimental demonstrations of these effects in a variety of laboratories [2–16]. The initial demonstration of interference [2] was carried out on a bound-bound transition in atomic mercury, driving concurrent one- and three-photon transitions between the same initial and final states and showing that the net transition probability could be modulated by varying the relative phase between the laser field components. Interference on bound-bound transitions has also been observed in small molecules [3] (HCl) and large molecules [4] (CH_3I, trimethyl amine, triethyl amine, NH_3, and cyclooctotetraene). There have been several demonstrations of interference using bound-free transitions in which angular distributions of products [5–8] or effective cross sections [9] have been controlled. The latter is typically achieved by interfering an even-order process with an odd-order process, while the former requires both processes to be of the same parity. Interference has been used to control photocurrents in unbiased semiconductors, in both intraband [10] and interband [11] transitions.

To date, there have been three reports of control of branching ratios using two-pathway interference [12–14]. The first [12] resulted from the interference between a three-photon process and a single-photon process in the molecule HI. Variation of the phase of the two field components allowed for the modulation of the fragment yields for HI^+ and $H + I^*$. Control of the branching ratio for these two product sets is increased in some wavelength ranges by a difference in phase for their modulation. Another form of interfering pathway control has been demonstrated by Shnitman *et al.* [13] using laser-induced-continuum structure effects. In this process, one laser field dissociates the molecule, while the second is tuned to a frequency that couples an initially unpopulated high-lying state to the continuum. The product-state distribution is highly sensitive to the frequency of the exciting laser field. This process is independent of the relative phase of the two laser fields.

In a recent work [14] we also reported observations of a phase-insensitive coherent control in which the interference between two two-photon ionization pathways in atomic barium was used to control the branching ratio between two ionization channels. This interference was observed by Pratt [16], who showed that it can lead to asymmetric line shapes in the photoionization of NO. Pratt suggested that this technique could be extended to control dissociation product distributions. In our work [14] each process involves the absorption of one photon of frequency ω_1 and one photon of frequency ω_2, where the frequencies ω_1 and ω_2 are nearly resonant with the $6s^2\,{}^1S_0 \rightarrow 6s6p\,{}^1P_1$ and $6s^2\,{}^1S_0 \rightarrow 6s7p\,{}^1P_1$ transitions in atomic barium, respectively. Thus there are two pathways to reach the continuum state at an energy $\varepsilon = \hbar(\omega_1 + \omega_2)$. Since the phase of a two-photon transition moment changes as the laser is tuned through an intermediate resonance, the line shape of the ionization rate as one laser is tuned through its resonance is very asymmetric, depending critically on the detuning of the other laser field from its intermediate resonance. Control of the branching ratio for different photoionization channels results since the moments for the processes differ, leading to different degrees of destructive interference. We observed the branching ratio change from 95% to 58% in tuning one laser from one side of resonance to the other. The range of detunings of the laser from resonance for which the asymmetry persisted, the strength of the interference, even under conditions where the magnitudes of the transition amplitudes for the two individual processes were not closely matched, and the reversed asymmetry of the spectra from that initially expected were also reported in that work. Being insensitive to the relative phase of the lasers, this coherent control technique is very robust. The beam alignment is not critical, nor is it important to carefully match beam sizes. In moving to dense media, as may prove necessary for useful application of these techniques, refractive index effects that modify the relative phase of the laser fields will not be a problem for this technique.

In this paper, we discuss further studies of this control process. We have investigated the dependence of the interference and the extent of control possible on atomic beam density, laser power, selection of intermediate states, and relative polarization of the two field components. In the following section we will describe the interference using argu-

*Present address: Intel Corp., Hillsboro, OR 97124-6497.

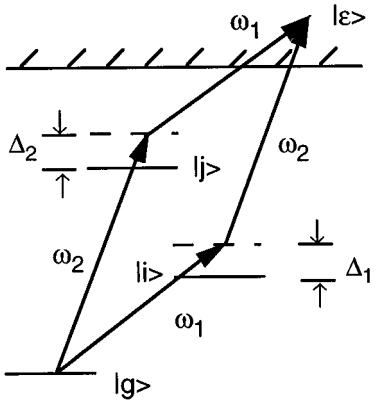

FIG. 1. Energy-level schematic showing the two interfering two-photon interactions. The atom absorbs one photon of frequency ω_1 and one photon of frequency ω_2 for both ionization routes.

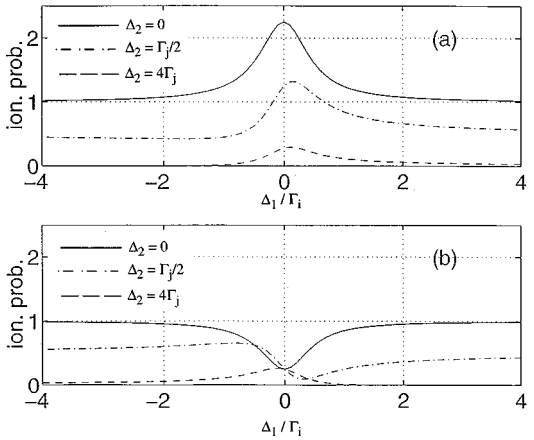

FIG. 2. Calculated line shapes for the interfering processes. In (a) the transition moments for the two interactions have the same sign, while in (b) they have the opposite sign.

ments based on a simple model of two-photon transition amplitudes. We will then describe in Sec. III the relevant features of atomic barium and describe why it is suitable for these initial studies. A detailed description of the experiment follows in Sec. IV and we present our results in Sec. V.

II. DESCRIPTION OF THE INTERFERENCE

Consider the two-photon interactions shown in the energy-level diagram in Fig. 1. One laser field, of amplitude E_1 and frequency ω_1, is tuned near the frequency ω_{ig} of the $|g\rangle \rightarrow |i\rangle$ transition. The second component of the laser field, of amplitude E_2 and frequency ω_2, is nearly resonant with the frequency of the $|g\rangle \rightarrow |j\rangle$ transition ω_{jg}. Thus there exist two resonantly enhanced pathways coupling the ground state to the continuum state of energy $\varepsilon = \hbar(\omega_1 + \omega_2)$. To lowest-order perturbation theory, the transition amplitude for one of these interactions is

$$T_1 = \frac{e^2}{\hbar} \frac{\vec{r}_{\varepsilon i} \cdot \vec{E}_2 \vec{r}_{ig} \cdot \vec{E}_1}{\Delta_1 + i\Gamma_i/2}, \tag{1}$$

where $e\vec{r}_{kl}$ represent the various transition dipole moments, $\Delta_1 = \omega_1 - \omega_{ig}$ is the detuning of the laser frequency from the resonance, and Γ_i is the width (full width at half maximum) of the intermediate state. The transition amplitude for the second process is of similar form:

$$T_2 = \frac{e^2}{\hbar} \frac{\vec{r}_{\varepsilon j} \cdot \vec{E}_1 \vec{r}_{jg} \cdot \vec{E}_2}{\Delta_2 + i\Gamma_j/2}. \tag{2}$$

While these expressions are not valid for strong fields or for resonant excitation, they still allow us to understand qualitatively the line shapes we should observe in these experiments. Since the two interactions are driven concurrently, the rate of photoionization into the continuum state of energy ε is given by the square of the sum of the individual transition amplitudes,

$$W \propto |T_1 + T_2|^2 = \frac{e^4}{\hbar^2} \left| \frac{z_{\varepsilon i} z_{ig}}{\Delta_1 + i\Gamma_i/2} + \frac{z_{\varepsilon j} z_{jg}}{\Delta_2 + i\Gamma_j/2} \right|^2 |E_1|^2 |E_2|^2. \tag{3}$$

Here we have written the transition rate for the specific case of both lasers linearly polarized and label this direction of polarization as the $\hat{z}$ axis. The coherence of the interaction is implicit in the form of Eq. (3), as the two-photon transition moments are summed before they are squared. The cross term leads to highly asymmetric ionization spectra as a function of, say, Δ_1, when $|\Delta_2| \sim \Gamma_j$.

By way of comparison, consider a similar interference between two two-photon interactions. This interference, which requires four laser fields, was suggested by Chen, Brumer, and Shapiro [17]. The atom or molecule can be ionized or dissociated by the two-photon interaction with field components of frequency ω_1 and ω_2, as shown in Fig. 1, or by a two-photon interaction with field components at frequencies ω_3 and ω_4, where $\omega_3 + \omega_4 = \omega_1 + \omega_2$. Each process is resonantly enhanced by different intermediate resonances and excites the system to a continuum state of the same energy $\varepsilon = \hbar(\omega_1 + \omega_2)$. Chen, Brumer, and Shapiro showed that the interference for the two-photon processes depends on the phase difference $\Delta\phi = (\phi_1 + \phi_2) - (\phi_3 + \phi_4)$, where ϕ_i is the phase of the field component at frequency ω_i. By varying $\Delta\phi$, the interference can be tuned through constructive and destructive conditions. The interference described in the present report is in fact a special case of the Chen-Brumer-Shapiro interference, in which $\omega_4 = \omega_1$ and $\omega_3 = \omega_2$. Then $\Delta\phi = (\phi_1 + \phi_2) - (\phi_2 + \phi_1) = 0$ and the sensitivity to the phase of the field components vanishes. Of course we also lose the ability to control the interaction by varying the relative phase of the fields, as has been demonstrated with other interfering interactions [2]. We can, however, vary the relative phase of the transition amplitudes by tuning the frequency of the laser fields, as has been demonstrated previously [14,16].

In Fig. 2 we display examples of Eq. (3) for the interfering line shape for photoionization as a function of detuning Δ_1 of laser 1. For this figure we have chosen the product of dipole moments for the process via level $|j\rangle$ to be twice that for the process via level $|i\rangle$. A distinct asymmetry is seen for all cases with the detuning comparable to the linewidth. Another manifestation of the interference is that the net transition rate when both lasers are resonant with their respective transitions is enhanced over the sum of the individual rates. For example, in Fig. 2 the rate for the interaction via level $|i\rangle$ is $|T_1|^2_{\Delta_1=0} = 0.25$, via level $|j\rangle$ is $|T_2|^2_{\Delta_2=0} = 1$, and with

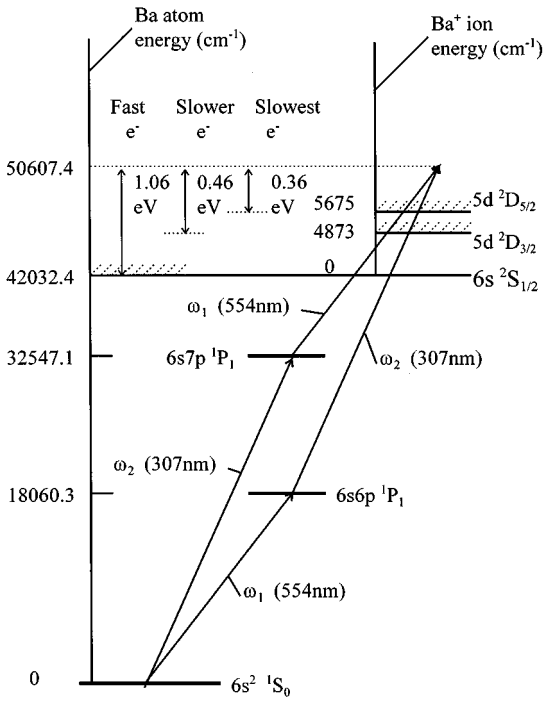

FIG. 3. Energy-level diagram for barium.

both transitions active it is $|T_1+T_2|^2_{\Delta_{1,2}=0}=2.25$. The line shapes for negative detunings, not shown in Fig. 2, have their asymmetry reversed from those for positive detunings. In Fig. 2(b) we show line shapes for the same parameters as used for Fig. 2(a), except the sign of the product of transition moments for one of the interactions is negative. This leads to destructive interference, so that, for example, the transition rate when both lasers are resonant with their respective transitions is $|T_1+T_2|^2_{\Delta_{1,2}=0}=0.25$.

The potential for coherent control of photoion state branching ratios is presented when multiple-ionization channels are accessed by the two-photon interactions. Since the transition dipole moments to the various continuum channels differ from one another, the interference can be exploited to enhance the selective access of one channel over the others. It is important to note that the interference can (and, in some cases, does) lead to asymmetric line shapes for the photoionization spectra without giving us control over the branching ratio. For example, if the spectra for the processes leading to the different ionization channels all have the same asymmetric line shapes, the interference does not enhance one product state over the others. In the experimental measurements shown and discussed in Sec. V, we will see examples of highly asymmetric line shapes, many of which lead to control and some of which do not.

III. ATOMIC STRUCTURE OF BARIUM

For this work we chose to work with atomic barium because of several advantageous features it offers. An energy-level diagram of barium showing some of the relevant states is shown in Fig. 3 [18]. The ground state of the barium atom, the $6s^2\,{}^1S_0$ state, has no fine or hyperfine structure to complicate the spectra. Its first-ionization limit is relatively low at 42 032.4 cm^{-1}, making possible two-photon ionization of the ground state with convenient wavelengths. The ground state of the core is the $6s\,{}^2S_{1/2}$ state. There are a pair of low-lying excited states of the core, the $5d\,{}^2D_J$ states, with $J=3/2$ or 5/2, which lie at 4873.850 cm^{-1} (0.605 eV) and 5674.824 cm^{-1} (0.704 eV) above the ground state of the ion, respectively. These continuum channels are also easily accessed in two-photon absorption from the ground state of the neutral atom. The next state of the ionic core is the $6p\,{}^2P_J$, which lies at a much higher energy (greater than 62 000 cm^{-1}), and is thus never produced in any of our measurements. The cross section for ionization is relatively flat and featureless in much of the spectral region between 47 707 cm^{-1} (the $^2D_{5/2}$ threshold) and 56 000 cm^{-1} [19]. Below this region, several Rydberg series of doubly excited autoionizing states leading to ^2D_J thresholds produce a rich spectrum, while at energies higher than this range, one encounters series of autoionizing resonances approaching the ^2P_J at an increasing spectral density [20]. We choose to work in this flat spectral region as often as possible so as to avoid complications that may be introduced by final-state resonances.

In the present experiments the two-photon processes involved are each resonantly enhanced by intermediate $6snp\,{}^1P_1$ states, where $n=6$, 7, or 8. Quantum-defect analysis of these states [21] shows that the $n=7$ and $n=8$ intermediate states are strongly mixed with several other electronic configurations, most significantly with $5dnp\,{}^1P_1$ states. The choice of intermediate state is important in that this determines the coupling to the different continuum states. For example, from our data presented in Sec. V, we see that the $n=7$ and $n=8$ intermediate states lead to much higher proportion of $5d\,{}^2D_{3/2,5/2}$ core states than does the $n=6$ intermediate state. This is understood in terms of the large admixture of the $6s7p\,{}^1P_1$ and $6s8p\,{}^1P_1$ with $5dnp\,{}^1P_1$ states.

Selection rules for dipole transitions limit the continuum states excited in our experiments to those with total orbital angular momentum L of 0 or 2 and total electronic angular momentum J of 0, 1, or 2. Since the initial ground state of neutral barium has even parity, only even wave functions in the continuum are excited by a two-photon interaction. In addition, while intercombination lines ($\Delta S=\pm 1$) are typically not as strong as $\Delta S=0$ lines, they are not negligible. Coherent optical excitation pathways interfere only when they connect the same initial and final states. While the ground state of barium is nondegenerate, the final states, being in the continuum, are a superposition of states listed in Table I and are simultaneously excited. For example, when the core state is the $6s\,{}^2S_{1/2}$, the photoelectron can find itself with $l=0$ or $l=2$. Additionally, the photoelectron may be in a singlet or a triplet state, depending on whether or not its spin was flipped during the ionization process. There are even more possible final states when the core is left in the $5d\,{}^2D_{3/2}$ or $5d\,{}^2D_{5/2}$ state. We expect the photoionization line shapes to have the greatest asymmetry when both excitation pathways lead most strongly to the same continuum state.

We have measured the angular distributions of the photoelectrons to help determine the potential for control. If these patterns differ significantly from one another, then the spatial overlap of the final-state wave functions is insufficient for strong interference or control of the total cross section for

TABLE I. Continuum states (*LS*-coupling terms) excited by two-photon ionization of barium.

$6s\,^2S_{1/2}$ core+ϵl photoelectron where ϵl and ^SL_J are		$5d\,^2D_{3/2,5/2}$ core+ϵl photoelectron where ϵl and ^SL_J are	
ϵs, $^1S_0$, or $^3S_1$			ϵs, $^1D_2$, or $^3D_{1,2}$
	ϵd, $^1D_2$, or $^3D_{1,2}$	ϵd, $^1S_0$, or $^3S_1$	ϵd, $^1D_2$, or $^3D_{1,2}$
			ϵg, $^1D_2$, or $^3D_{1,2}$

excitation into that state. We will describe in detail how we carry out these angular distribution measurements in Sec. IV. In short, we can select one of the follow interactions:

$$6s^2\,^1S_0 \rightarrow 6snp\,^1P_1 \rightarrow \begin{cases} 6s\,^2S_{1/2}+e^- \\ 5d\,^2D_{3/2}+e^- \\ 5d\,^2D_{5/2}+e^-, \end{cases} \tag{4}$$

where n is 6, 7, or 8, and determine the photoelectron flux as a function of θ, the angle between the laser polarization and the direction of propagation of the photoelectron. The angular distributions are shown in Fig. 4, where θ is the angle with respect to the vertical axis. The data points represent our measured photoelectron fluxes and the solid line is the result of a least-squares fit to the equation

$$\frac{\partial\sigma}{\partial\Omega} = a_0[1 + a_2\cos(2\theta) + a_4\cos(4\theta)]. \tag{5}$$

The six plots on the left-hand side are taken with the UV laser near 307 nm, while those on the right-hand side are with $\lambda_2 \sim 279$ nm. The top row contains the distributions for the fastest photoelectrons, ejected when the Ba^+ core is left in $6s\,^2S_{1/2}$ state. The second and third are for the slow electrons, with the core left in the $5d\,^2D_{3/2}$ and $5d\,^2D_{5/2}$ states, respectively. The asymmetry in some of these measurements can be attributed to a slight degree of elliptical polarization of the laser fields. While a detailed analysis must wait for more precise measurements, we are able to draw some conclusions from the plots shown in Fig. 4. For example, the two distributions in the top row on the left are for the fast photoelectrons that are photoionized via the $n=6$ and $n=7$

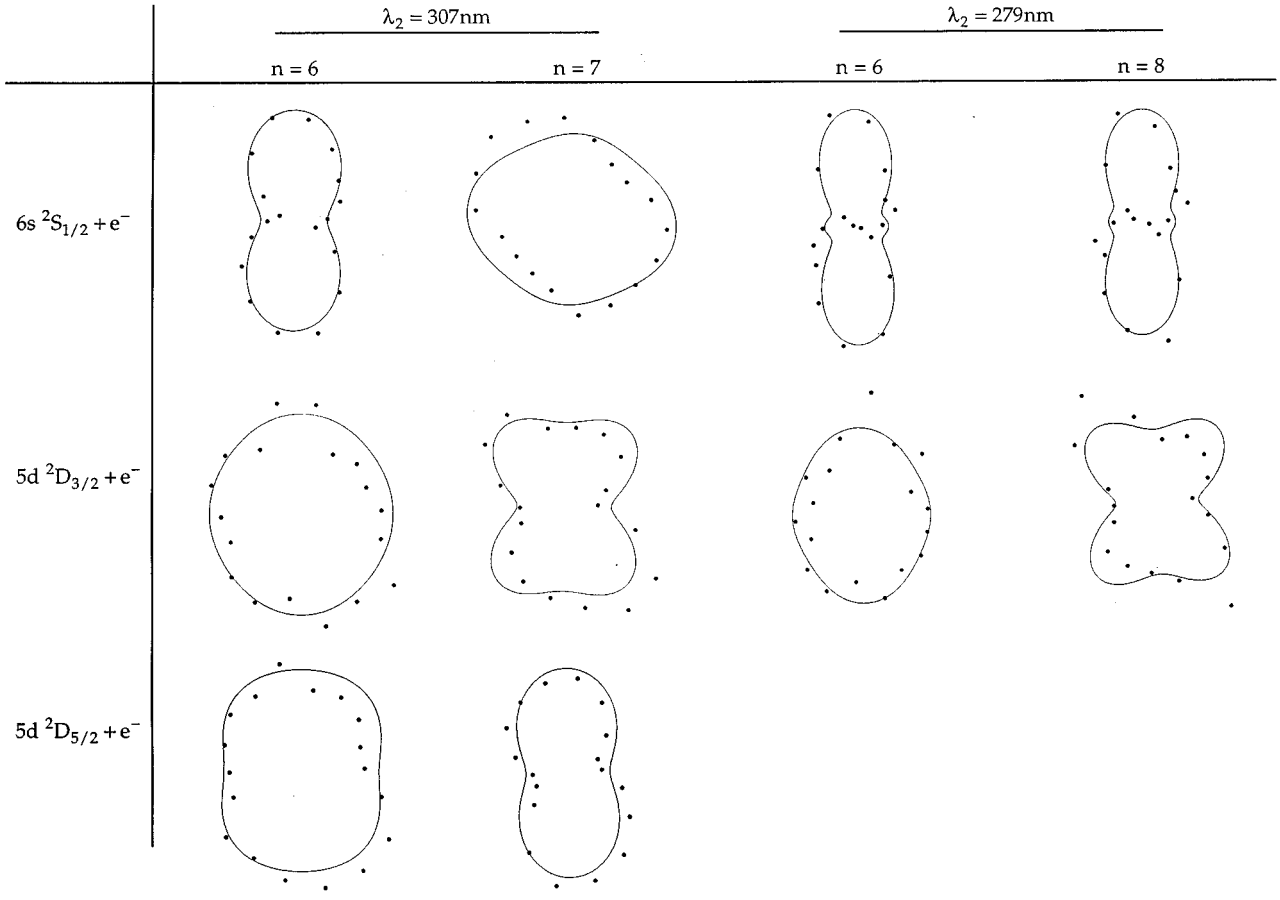

FIG. 4. Photoelectron angular distributions for two-photon ionizaton of atomic barium. The interactions are described in Eq. (4). The laser polarization is vertical for these figures and the radius of each data point indicates the relative flux of photoelectrons in that direction. The solid line is the result of a least-squares fitting procedure to an equation of the form given by Eq. (5).

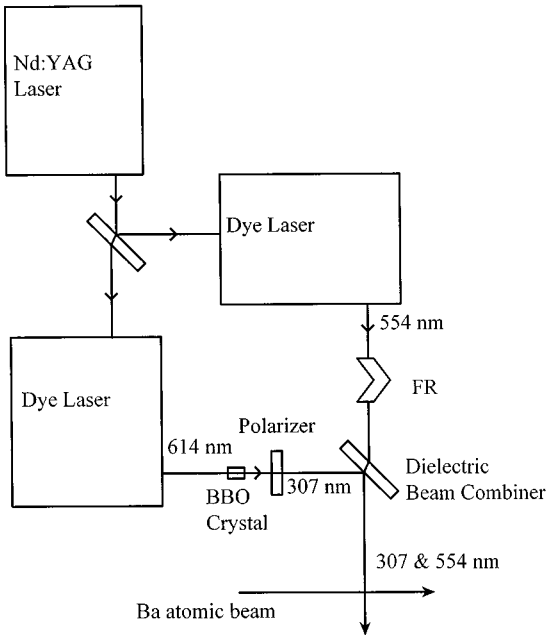

FIG. 5. Diagram of the experimental setup. Two dye lasers are pumped by the frequency doubled output of a Nd:YAG laser. The polarization of the green beam is oriented using the Fresnel rhomb (FR).

intermediate states. When $\lambda_1=554$ nm and $\lambda_2=307$ nm are tuned near their respective transitions, we can observe the interference between these two interactions. These distributions, however, show that the two interactions lead to angular momentum states of the photoelectron that are somewhat different from one another. The distribution through the $n=7$ state is nearly isotropic, while that for the $n=6$ intermediate state shows a strong maximum in the direction of the laser polarization. On the basis of this comparison, we should not expect to see strong interference for these signals. We might expect to see better interference, however, for the slow electron signals, as these angular distributions are a bit more similar. When the UV laser is tuned to the $n=8$ intermediate state at $\lambda_2=279$ nm, the photoelectron angular distributions for the fast electrons are very similar to one another, as shown by the two distributions on the right-hand side of the top row. This would indicate that we may see a stronger interference on the fast electron signal here than at $\lambda_2=307$ nm. It is clear that a more detailed analysis will be required to fully understand these interferences. In Sec. IV we will describe the measurement techniques we used for observing the interference, as well as those for making the photoelectron angular distribution measurements shown in Fig. 4.

IV. EXPERIMENT

A schematic diagram of the experimental setup is shown in Fig. 5. Two tunable dye lasers (pulse duration ~ 15 nsec) are pumped by the second harmonic (532 nm) of a Q-switched Nd:YAG laser (where YAG denotes yttrium aluminum garnet), producing 1.5 mJ of radiation at $\lambda_1\approx 554$ nm and 10 mJ pulse energy at $2\lambda_2\approx 614$ nm or $2\lambda_2\approx 557$ nm. The $2\lambda_2$ radiation is frequency doubled, producing up to 200 μJ pulse energy at 307 nm or 279 nm. The wavelength λ_1 is in near resonance with the $6s^2\,{}^1S_0\rightarrow 6s6p\,{}^1P_1$ transition, while λ_2 is near the $6s^2\,{}^1S_0\rightarrow 6s7p\,{}^1P_1$ transition (307 nm) or the $6s^2\,{}^1S_0\rightarrow 6s8p\,{}^1P_1$ transition (279 nm). Both lasers produce 1–3 longitudinal modes, with a mode spacing of ~ 3 GHz in the UV and 0.5 GHz for the green. The two laser beams are collimated, combined, and crossed at a right angle with an effusive beam of barium atoms (atom beam diameter equal to 2 mm and background vacuum pressure equal to 2×10^{-8} torr). We varied the density of the atomic beam [22] (as determined from the junction voltage of a chromel-alumel thermocouple mounted on the oven and vapor pressure curves for barium) from 0.33×10^7 to 5.8×10^7 cm^{-3}. (The systematic error in the density may be as large as a factor of 2, as the vapor pressure depends strongly on the oven temperature.) The diameter of the nearly Gaussian shaped laser beams is ~ 1 mm and their timing is carefully measured by a photodiode detector and adjusted to match each other. The peak intensities of these beams in the interaction region are 2×10^7 W cm^{-2} in the green and 3×10^6 W cm^{-2} in the UV. Under these conditions, we observe absorption linewidths of up to 6 cm^{-1}, dominated by power broadening of the transition by the green laser. We calibrate the wavelength of the UV light by observing the ionization spectrum at low intensities, where the Stark shift of the atomic transition frequency is expected to be small. We estimate the Stark shift to be about 1.6 cm^{-1} when the pulse energy of the green beam is 1.5 mJ.

Upon absorption of one photon from each laser beam, three photoionization channels (not including different angular momentum states of the ejected electron) are accessed: The Ba^+ core may be in its ground $6s\,{}^2S_{1/2}$ state or in a $5d\,{}^2D_{3/2}$ or $5d\,{}^2D_{5/2}$ state. For $\lambda_2\approx 307$ nm (279 nm), the corresponding photoelectron energies are 1.06 eV (1.48 eV), 0.46 eV (0.87 eV), and 0.36 eV (0.77 eV), respectively. Thus the relative excitation probabilities of the different core states can be determined by photoelectron time-of-flight (TOF) measurements. In order to increase collection efficiency and to minimize the sensitivity of our measurements to variations in the photoelectron angular distributions, we have constructed an ellipsoidal electron mirror, shown in Fig. 6, which is designed to collect all the electrons that are ejected into the lower half space. The electron mirror consists of a pair of (nonmagnetic) nickel-plated ellipsoidal meshes. The meshes have an 81% open area to allow high transmission of the electrons. The nickel plating makes the meshes semirigid, so that they can retain their ellipsoidal shape with minimal extra support. The inner mesh is at ground potential, while the outer mesh is biased at a small negative potential, typically -3 V. Any electrons ejected into the lower half space penetrate the first mesh and are repelled by the potential gradient in the space between the meshes. With the interaction region at one focus of the ellipsoid, the electrons are focused by the electron mirror onto the other focus of the ellipsoid. The path length of the electron trajectory from the interaction region to the opposing focus is 18.0 cm. A 1-cm-radius aperture at the upper focus allows these electrons access to a two-stage microchannel plate (MCP) electron multiplier and the amplified electron signal is collected on a biased anode. The entire flight path is shielded to minimize electrostatic and magnetostatic fields, which, if present, might distort the trajectory of the electrons. Electrostatic shielding is provided by enclosing the volume with a

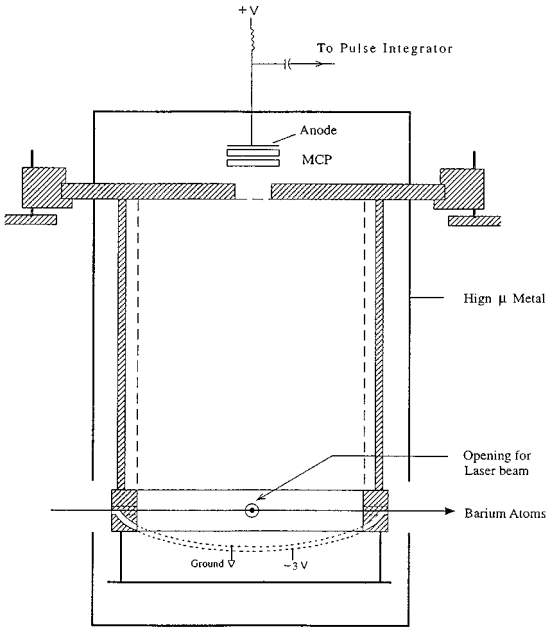

FIG. 6. Diagram of the ellipsoidal electron mirror. The atom beam and the laser beams cross at the lower focus of the ellipsoid, while the other focus is at the aperture in the top plate. The electron signal is multiplied in the microchannel plate (MCP) and collected on the anode.

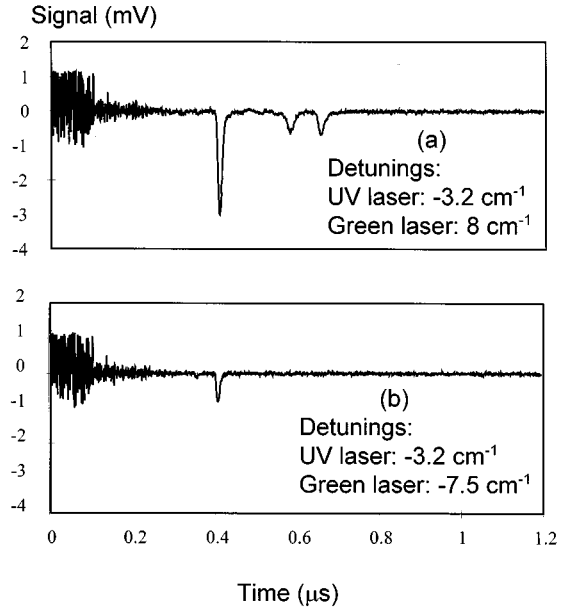

FIG. 7. Two time-of-flight spectra of the photoelectrons. In (a) the laser detunings are $\Delta_1 = 8.0\ \mathrm{cm}^{-1}$ and $\Delta_2 = -3.2\ \mathrm{cm}^{-1}$, while in (b) they are $\Delta_1 = -7.5\ \mathrm{cm}^{-1}$ and $\Delta_2 = -3.2\ \mathrm{cm}^{-1}$.

grounded stainless-steel mesh, nickel plated to reduce the contact potential at the junction with the inner mesh of the electron mirror. The 1-cm aperture at the top plate is covered by a grounded mesh to reduce stray fields from the MCP leaking into the field-free region. Magnetic fields are reduced to below 10 mG using a three-dimensional configuration of current loops (whose spacing is twice that of a Helmholtz pair) and also by using μ-metal shielding.

To determine if our electron mirror collects the downward ejected photoelectrons with high, uniform efficiency, we have performed two tests. First, we compare the magnitude of the signal corresponding to the photoelectrons that are reflected by the electron mirror toward the detector with that of the photoelectrons that travel directly from the interaction region to the detector without being reflected by the electron mirror. These signals are easily identified by their flight time. The magnitude of the reflected electron signal is typically larger than the direct signal by a factor of 100 or more. The solid angle of the detector aperture is $\sim 0.004\pi$ sr, while that of the electron mirror is 2π sr. It is difficult to be any more quantitative in this comparison since the direct electron signal is not isotropic. Our second set of tests of the electron mirror is a series of observations of the photoionization signal taken as we rotate the direction of polarization of a one-color ionizing laser field. In order to test the mirror at a variety of photoelectron kinetic energies, we have carried out this measurement at three different wavelengths: 708.46 nm, 579.81 nm, and 559.25 nm. With the laser tuned to 708.46 nm the $6s7s\ ^1S_0$ serves as the two-photon resonant intermediate state and the kinetic energy of the photoelectrons is 39 meV. For this very low electron kinetic energy, we must decrease the potential on the outer mesh of the electron mirror from -3 V to ~ -100 mV. The flight time of these electrons is 1.5 μsec, as expected, but the TOF peak is somewhat broad (~ 0.3 μsec). This is perhaps evidence of small stray fields within the free-flight region. At 579.81 nm, an intermediate $6p^2\ ^3P_0$ state enhances the ionization process, leading to photoelectrons of energies 1.20 eV, 0.60 eV, and 0.50 eV. Finally, we use the $6s7d\ ^3D_2$ state, two-photon resonant at 559.25 nm, ejecting photoelectrons with energies of 1.44 eV, 0.84 eV, and 0.74 eV. At each of these wavelengths, we rotate the polarization of the incident light with a half-wave Fresnel rhomb and measure the modulation of the ionization signals. The modulation of the angle-integrated signal is less than 10% of the average value for all but the lowest photoelectron energy used. For 39-meV photoelectrons, however, the signal shows strong variation with the laser polarization direction, suggesting that only a small portion of the electron mirror is able to focus these extremely low-energy photoelectrons toward the detector. Since the photoelectron angular distributions for these interactions are all strongly directional, we conclude that the electron mirror is able to collect electrons ejected into the lower half space with uniform efficiency for a broad range of kinetic energies, but not for low energies where electron trajectories are easily perturbed.

We measure the time-of-flight spectrum of the photoelectrons using either gated pulse integrators or a digitizing oscilloscope. Sample TOF spectra, taken with $\lambda_2 \sim 307$ nm, are shown in Fig. 7. These traces represent the averages of the photoelectron signal taken over 100 pulses of the lasers. The principal peaks are at 1.06 eV, 0.46 eV, and 0.36 eV. The width of the fast and slow electron peaks are typically 25 nsec and 35 nsec, respectively. The fast electron peak in this oscilloscope trace has an amplitude of 3 mV. Since the gain of the microchannel plate detector is $\sim 1 \times 10^6$ (at a bias voltage of 1640 V), this signal corresponds to an average of 10 detected photoelectrons per laser pulse. Barely discernible from the noise are pulses due to direct electrons, which we defined earlier as those electrons that travel directly to the detector without being reflected from the electron mirror.

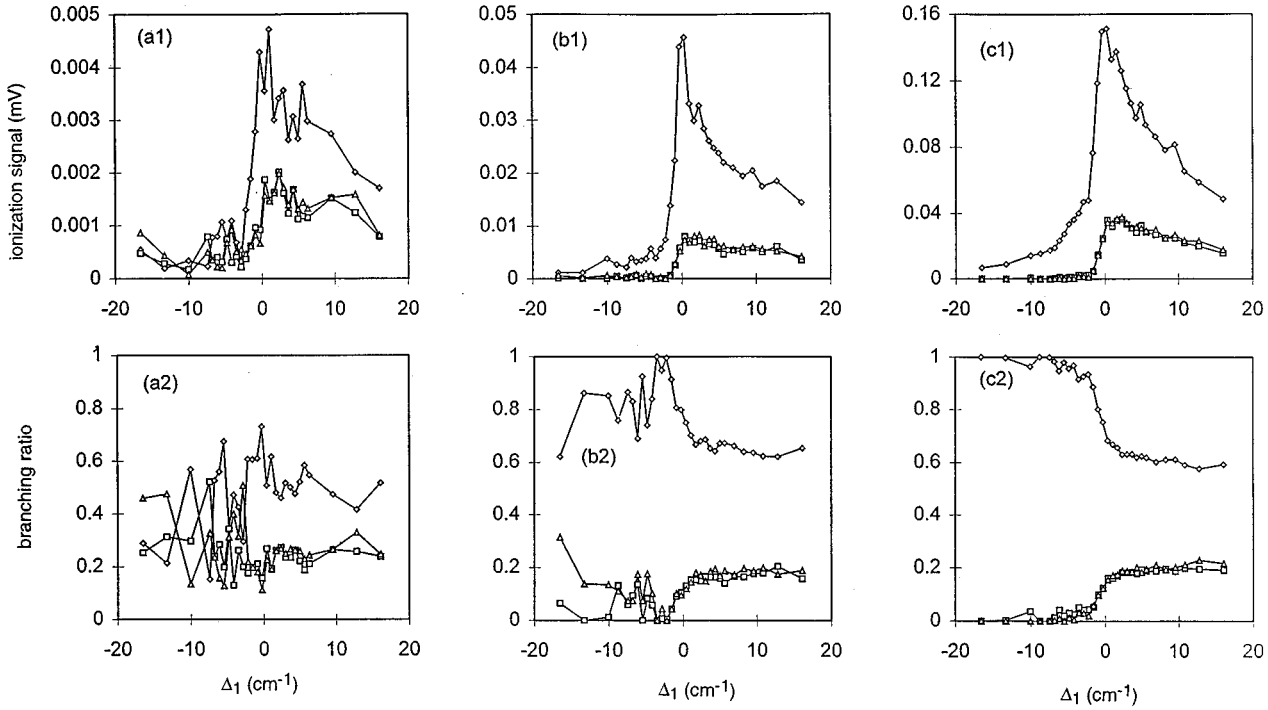

FIG. 8. Measured two-photon ionization line shapes (a1)–(c1) and branching ratios for the different ionization channels (a2)–(c2) as functions of the detuning of the green laser. The density of the barium is 0.33, 1.4, and 5.8×10^{7} cm^{-3} in (a), (b), and (c), respectively. The symbols represent the following core states: $6s\,^2S_{1/2}$, ◇; $5d\,^2D_{3/2}$, □; and $5d\,^2D_{5/2}$, △. The detuning of the UV light is $\Delta_2=-3.2$ cm^{-1}.

When we increase the laser pulse energy of the green laser to 5 mJ, we are also able to observe peaks at 1.51 eV, 0.91 eV, and 0.81 eV. These result from three-photon ionization of the barium by the 554-nm field. Finally, in some of the TOF spectra, we are able to observe a peak at 0.52 eV. We have determined that this peak results from the photoionization by the 554-nm beam of the $6s7s\,^1S_0$, which is populated by decay from the $6s7p\,^1P_1$ state. We observe resonances in this peak when the green laser is tuned into resonance with transitions to the $5d17p\,^3P_1$ and $5d17p\,^3D_1$ autoionizing states. The line shape of this peak also shows the effects of this interference, indicating that the interference influences the population of the intermediate $6s7p\,^1P_1$ state.

This configuration of our appararus also allows us to measure the angular distributions of the photoelectrons. We discussed the results of these measurements in Sec. III. We choose the intermediate state by tuning the lasers to the resonant frequency of the transition from the ground state and the final state by selecting the appropriate peak in the TOF spectrum. As we do not want any interferences to contribute to these angular distributions, either the green or UV laser is tuned far enough off resonance that the two-photon ionization process can proceed via only one intermediate resonance. The photoelectron angular distribution measurements are recorded by turning off the repulsive bias on the bottom mesh of the ellipsoidal electron mirror and collecting only the direct photoelectrons with the MCP detector. We rotate the laser polarization using a $\lambda/2$ Fresnel rhomb and determine the photoelectron peak area for the three peaks in the TOF spectrum. The Fresnel rhomb is, unfortunately, not perfectly achromatic in its phase retardation, since the phase shift of the s- and p-polarization components depends on the refractive index of the material from which the rhomb is constructed, and the refractive index is, of course, wavelength dependent. Our rhomb is of fused silica, with an angle of incidence of 51°. We estimate that the phase shift differs by $\sim0.05\pi$ between the different beams, so that the polarization of the output beams is not perfectly linearly polarized. Still, the measured distributions shown in Fig. 4 are sufficient to allow a qualitative comparison.

With the apparatus described in this section, we have measured the dependence of the photoionization line shapes, and of the control of the branching ratio, on various experimental parameters at our disposal. These parameters include the density of the atomic beam, the pulse energies of the lasers, the choice of intermediate resonant states, and the laser polarization. In the following section, we will discuss in detail the results of these measurements.

V. RESULTS

A. Density of the atomic beam

We have measured the photoionization spectra and branching ratio for three different atomic-beam densities. These data are all recorded with the UV laser tuned near the $6s^2\rightarrow6s7p$ transition (i.e., $\lambda_2\sim307$ nm). In Fig. 8 we show these data for a detuning from resonance of $\Delta_2=-3.2$ cm^{-1}. The polarization of the two field components are parallel to one another and the pulse energies are 530 μJ at 554 nm and 65 μJ at 307 nm. The atomic-beam densities in these plots are, from left to right, 0.33×10^{7}, 1.4×10^{7}, and 5.8×10^{7} cm^{-3}. Since the interaction volume is ~2 mm^3, there are about 0.7×10^{4}, 2.8×10^{4}, and 11.6×10^{4} atoms,

respectively, in the interaction region. At each density, the photoionization line shapes display a clear asymmetry. It is interesting to note, however, that the branching ratios for the different photoionization channels are very dependent on the density of the atomic beam. At the lowest density, the branching ratio shows little variation with detuning of either laser field from resonance. The signal level at this density is so small that it is barely above that of the noise. For a density of 1.4×10^{7} cm^{-3} [Fig. 8(b)], however, the asymmetric line shapes lead us to a very clear control. Nearly all of the ions are in the ground state for $\Delta_1<0$ since the destructive interference of the slow electron peaks is very strong. For $\Delta_1>0$, however, only 60% of the ions are in their ground state. An interesting observation comes from the data for $\Delta_2=\pm 9.6$ cm^{-1}, not shown in Fig. 8, for which the pathway that uses the $6s7p$ intermediate resonance is nearly closed. Here the fast electron peak becomes very symmetric, while the asymmetry of the slow electron peak is still quite pronounced.

At the highest beam density of this study (5.8×10^{7} cm^{-3}), our ability to control the branching ratio is further increased. The width and asymmetry of the photoionization spectra are greater than observed for the lower densities, with nearly complete suppression of the slow electron signal for $\Delta_1<0$ for the case $\Delta_2=-3.2$ cm^{-1}. The corresponding signal for the fast electrons also shows destructive interference, but the suppression is not nearly so complete. Thus we see that nearly 100% of the photoions are left in the ground $6s\,^2S_{1/2}$ state. This is also illustrated in Fig. 7, in which the TOF spectra of the photoelectrons correspond to two different sets of laser detunings. The detuning of the UV beam is the same ($\Delta_2=-3.2$ cm^{-1}) in Figs. 7(a) and 7(b), while Δ_1 differs [8.0 cm^{-1} in Fig. 7(a) and -7.5 cm^{-1} in Fig. 7(b)]. These spectra are a clear demonstration of control of the product distribution by tuning only one laser frequency.

Finally, measurements that we reported in our initial report [14] of this phase-insensitive control were carried out at a density of 8.6×10^{7} cm^{-3}. The comparison of these data is made somewhat indirect in that the laser pulse energies are also different (1.5 mJ at 554 nm and 25 μJ at 307 nm), but still we note that the peak asymmetry and branching ratio control are even greater at this highest beam density.

In conclusion, with increasing density of the barium beam, we observe an increased capacity for control. The photoionization spectra show the strongest asymmetry at the largest density of our observations, often with complete destructive interference to one side of resonance. At $\rho=5.8\times10^{7}$ cm^{-3}, the interference persists to detunings of the green laser as large as $\Delta_1=17$ cm^{-1} in some cases, the maximum detuning we used in our experiments. This implies that the barium atoms are not acting independently of one another, but rather are participating in some sort of collective behavior, perhaps by coupling the two laser field components to one another through their nonlinear interaction. If each barium atom were acting independently of all the others, then we would expect the photoionization line shapes to increase linearly with the atom-beam density, but to retain the same shape. This is clearly not consistent with our observations, as is evident from the spectra of Fig. 8. While it is perhaps not surprising that the density of the atoms is important in these interactions, it is surprising that the density plays such an important role at these low densities. For example, the absorption length for the 554-nm light at line center (a linear process) at a density of 5.8×10^{7} cm^{-3} is 35 cm (determined by estimating the absorption cross section by $\lambda^2/2\pi$). The diameter of the atomic beam (2 mm) is smaller than this absorption thickness by a factor of 175. We do observe that the magnitude of the noninterfering photoionization signals for both the fast and slow electrons increases linearly with atomic beam density. This is observed by tuning one laser or the other off resonance such that only one photoionization pathway remains. With both lasers near resonance, however, the density dependence of the photoelectron signal becomes very complicated due to the interference. It will be interesting in future studies to look for changes to the laser fields affected by the interference phenomenon [15,23]. At this point, however, the only firm conclusion we can draw is that these complex interactions allow us an increased capacity for control with increasing atomic-beam density.

B. Laser pulse energy

Laser pulse energy also has a very pronounced effect on the control process. We measured the dependence of the interference on the pulse energies of the green and UV laser beams. The photoionization line shapes change in a very unusual manner in these studies. In all our studies of the pulse energy dependence, the laser polarizations are parallel to one another and the barium beam density is $\rho=5.8\times10^{7}$ cm^{-3}.

In the first set of data, we fixed the pulse energy of the UV laser at 62 μJ and measured the photoionization spectra for pulse energies of the green laser at 590 μJ, 150 μJ, and 44 μJ. We show the photoionization spectra and branching ratios for the case $\Delta_2=-3.4$ cm^{-1} in Fig. 9 and for $\Delta_2=0$ in Fig. 10. For large values of Δ_2 such that the two-photon interaction via the $6s6p$ intermediate state dominates that via the $6s7p$, the signal strength at the peak of these spectra is nearly independent of the pulse energy of the green laser, indicating that the $6s^2\rightarrow6s6p$ transition is strongly saturated for all pulse energies used in this work. A similar comparison of the signal strength in the wings of the $\Delta_2=0$ spectra, where the two-photon resonance via the $6s7p$ state dominates, indicates that the photoionization of the $6s7p$ state by the green laser is nearly linear in the laser energy.

We see a strong dependence of the asymmetry of the photoionization spectra and of the branching ratio curve on pulse energy. When the pulse energy of the green laser is 590 μJ, the conditions are similar to those described in Sec. V A and we observe spectra that are highly asymmetric and branching ratios of the photoion states that differ significantly as a function of the detunings of the lasers from their respective resonances. We show an example of this in Fig. 9(a). When we tune the UV frequency to its resonance, $\Delta_2=0$, the photoionization spectra for fast and slow electrons each reach a local minimum at $\Delta_1=0$, as shown in Fig. 10(a). When the laser energy is decreased to 150 μJ, however, the asymmetry of the curves only becomes obvious for $|\Delta_2|<2.5$ cm^{-1}. The spectra in Fig. 9(b), where $\Delta_2=-3.4$ cm^{-1}, appear highly symmetric. The clearest examples of product control at this pulse energy occur for $|\Delta_2|\sim2$ cm^{-1},

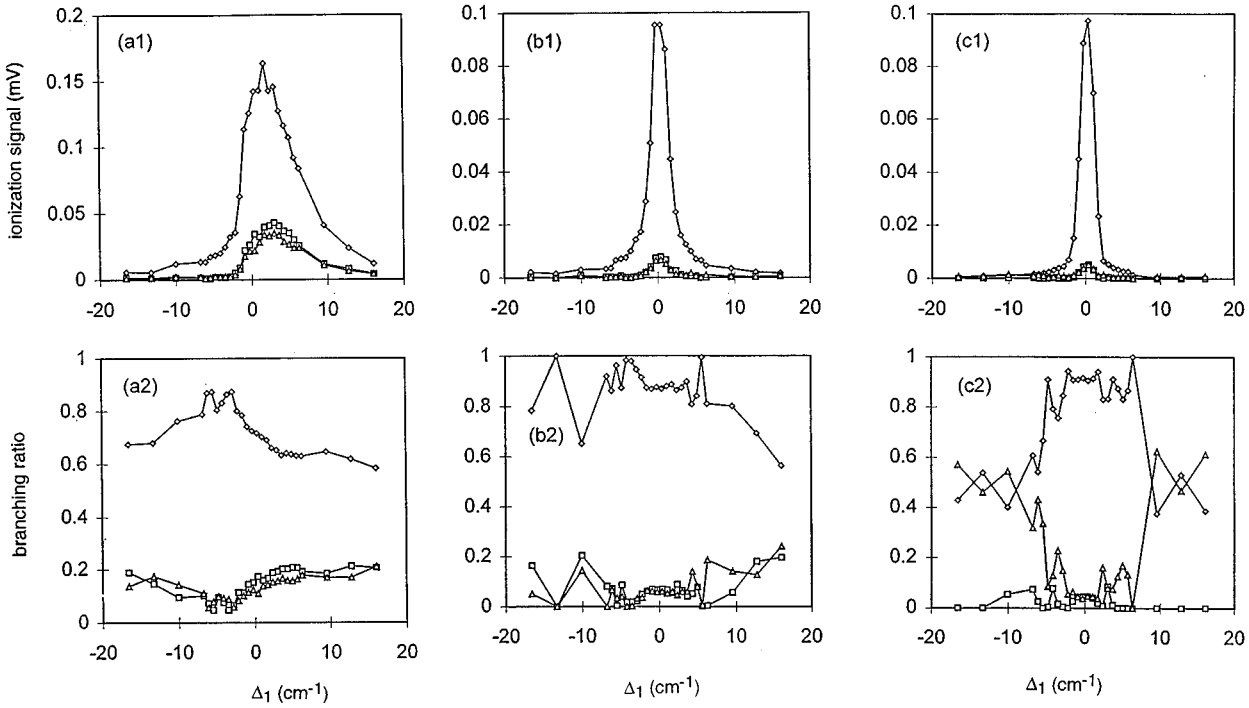

FIG. 9. Measured two-photon ionization line shapes (a1)–(c1) and branching ratios for the different ionization channels (a2)–(c2) as functions of the detuning of the green laser. The pulse energy of the green laser is 590, 150, and 44 μJ in (a), (b), and (c), respectively. The symbols represent the following core states: $6s\,^2S_{1/2}$, $\diamond$; $5d\,^2D_{3/2}$, $\square$; and $5d\,^2D_{5/2}$, $\triangle$. The detuning of the UV light is $\Delta_2=-3.4$ cm^{-1}.

but the frequency range over which the branching ratio is influenced by the interference is decreased. Also of interest is the spectra for $\Delta_2=0$, shown in Fig. 10(a), where it can be seen that the fast electron spectrum reaches a local maximum at line center, in contrast to the higher intensity data, which yielded a local minimum at this point. The peak signal of the fast electron spectra does reach a local minimum, however, if one examines the signal as a function of Δ_2. Finally, we

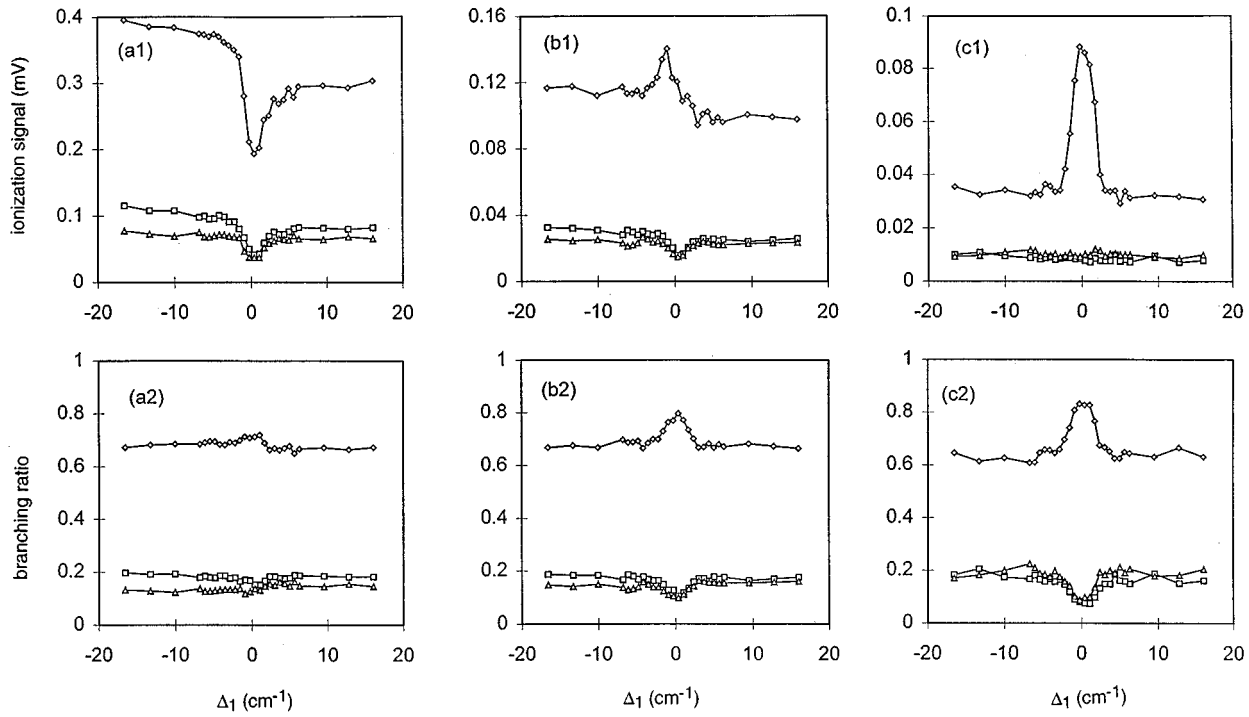

FIG. 10. Measured two-photon ionization line shapes (a1)–(c1) and branching ratios for the different ionization channels (a2)–(c2) as functions of the detuning of the green laser. The pulse energy of the green laser is 590, 150, and 44 μJ in (a), (b), and (c), respectively. The symbols represent the following core states: $6s\,^2S_{1/2}$, $\diamond$; $5d\,^2D_{3/2}$, $\square$; and $5d\,^2D_{5/2}$, $\triangle$. The detuning of the UV light is $\Delta_2=0$ cm^{-1}.

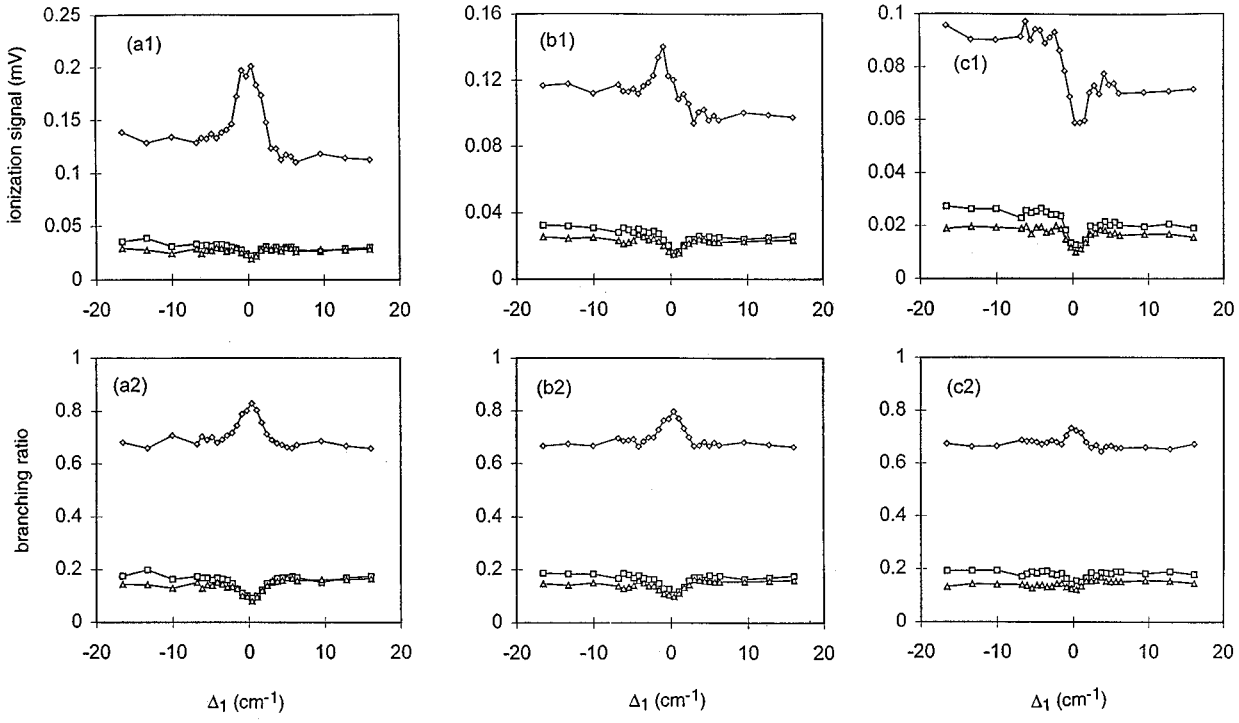

FIG. 11. Measured two-photon ionization line shapes (a1)–(c1) and branching ratios for the different ionization channels (a2)–(c2) as functions of the detuning of the green laser. The pulse energy of the UV laser is 200, 62, and 14 μJ in (a), (b), and (c), respectively. The symbols represent the following core states: $6s\,^2S_{1/2}$, $\diamond$; $5d\,^2D_{3/2}$, $\square$; and $5d\,^2D_{5/2}$, $\triangle$. The detuning of the UV light is $\Delta_2=0$ cm^{-1}.

lowered the pulse energy of the green laser to 44 μJ. At this energy, the photoionization spectra appear symmetric for all Δ_2. The data in Fig. 9(c) are recorded for $\Delta_2=-3.4$ cm^{-1}. Signatures of the interference do appear in the branching ratio plots, however, as shown, for example, in the curves of Fig. 10(c). The slow electron spectrum is nearly independent of Δ_1, while the fast electron spectrum shows a strong peak at line center.

We have also recorded the two-pathway interfering photoionization spectra as functions of the intensity of the UV laser. In these studies, the laser pulse energy of the UV laser is 200 μJ, 62 μJ, or 14 μJ. Samples of these spectra, taken at $\Delta_2=0$, are shown in Figs. 11(a), 11(b), and 11(c), respectively. The pulse energy of the green laser is 150 μJ in each case. As with the measurements described above, the laser polarizations are parallel to one another and the barium beam density is $\rho=5.8\times10^7$ cm^{-3}. These measurements again help us determine the degree of saturation of the individual steps of these two-photon processes. For large values of Δ_2, the signal strength at the peak of these spectra increases with increasing pulse energy of the UV laser, but at a rate that is less than linear. This indicates that the photoionization of the $6s6p$ state by the UV laser is approaching saturation levels. The signal strength in the wings of the $\Delta_2=0$ spectra change by less than a factor of 2 over this broad range of UV pulse energies, showing that $6s^2\rightarrow6s7p$ transition is nearly saturated. The spectra for UV energies of 200 μJ are very symmetric and the branching ratios show that the fast electrons are more probable near line center. The spectra for the fast electrons at $\Delta_2=0$, shown in Fig. 11(a), reach a maximum at line center, while that for the slow electrons is relatively flat. With decreasing UV pulse energy, however, the asymmetry of the spectra increases. The $\Delta_2=0$ spectra shown in Figs. 11(b) and 11(c), show that the maximum in the fast electron peak becomes a minimum for UV pulse energies of 62 μJ and 14 μJ.

In conclusion, the line shapes and control strongly depend on the laser pulse energies of the two lasers. When the green laser is much stronger than the UV laser, the detuning line shapes go through dips for both fast and slow electron signals when both lasers are resonant with their respective transitions. When the two laser energies are comparable, however, the fast electrons show a peak in the spectra, while the slow electron signals become flat.

C. Change of intermediate-state resonance

In this section we discuss the effect of changing the intermediate states for the two interfering processes. All of the results we have discussed in the previous sections were recorded with the UV laser tuned to the $6s^2\,^1S_0\rightarrow6s7p\,^1P_1$ transition. By changing this laser frequency to be nearly resonant with the $6s^2\,^1S_0\rightarrow6s8p\,^1P_1$ transition at a wavelength of $\lambda_2=279$ nm, we have determined that our initial choice of intermediate resonances that lead to interference is not unique. In Fig. 12(a) we show one example ($\Delta_2=-1.0$ cm^{-1}) of these spectra and the corresponding plot of the branching ratio. The laser pulse energies for these spectra are 280 μJ (green) and 70 μJ (UV), the density of the atomic barium is $\rho=5.8\times10^7$ cm^{-3}, and the laser polarizations are parallel to one another. The asymmetry of the fast electron peak is very slight and in almost every respect these spectra resemble the data taken with the UV laser at $\lambda_2=307$ nm with laser pulse energies of 44 μJ and 62 μJ for the green and UV lasers, respectively. The fast electron signal has a maximum at $\Delta_1=0$ for all values of Δ_2. The slow electron

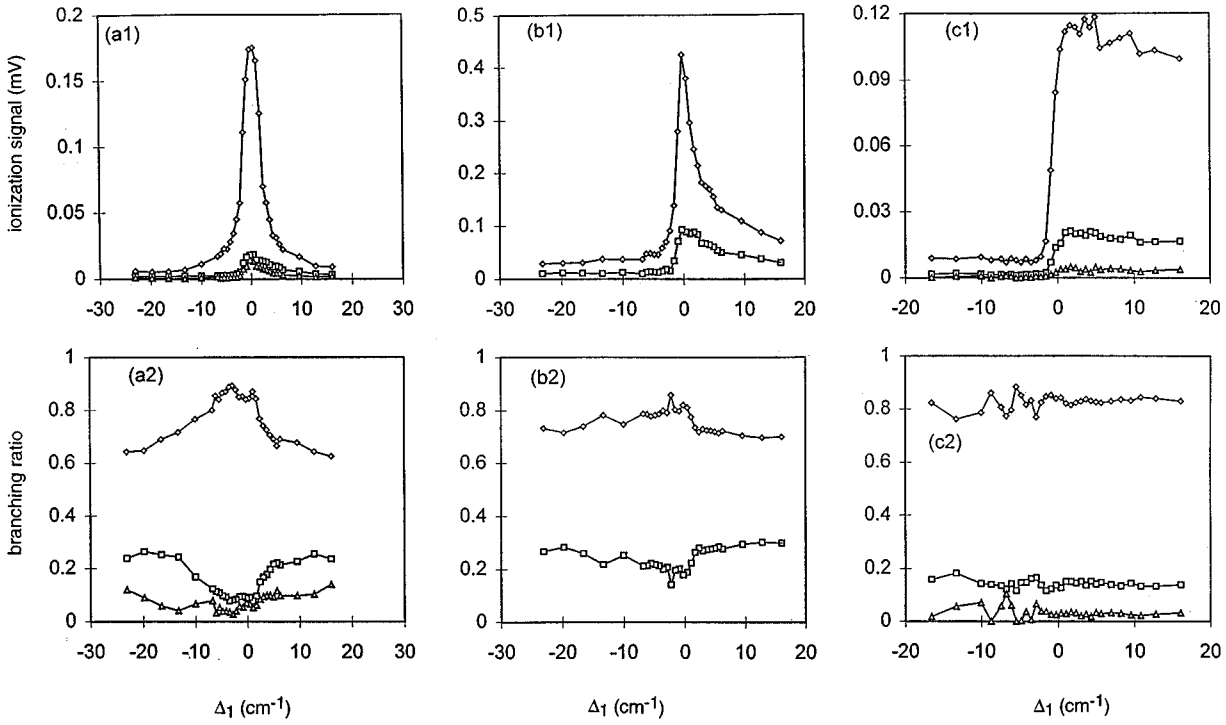

FIG. 12. Measured two-photon ionization line shapes (a1)–(c1) and branching ratios for the different ionization channels (a2)–(c2) as functions of the detuning of the green laser. The wavelength of the UV laser, relative polarization of the two laser fields, and detuning Δ_2 for the plots are (a) $\lambda_2=279$ nm, parallel polarizations, $\Delta_2=-0.7$ cm^{-1}; (b) $\lambda_2=279$ nm, perpendicular polarizations, $\Delta_2=-1.0$ cm^{-1}; and (c) $\lambda_2=307$ nm, perpendicular polarizations, $\Delta_2=-0.7$ cm^{-1}. The symbols represent the following core states: $6s\,^2S_{1/2}$, $\diamond$; $5d\,^2D_{3/2}$, $\square$; $5d\,^2D_{5/2}$, $\triangle$.

signal has a slight dip at $\Delta_2=0$. In view of the strong dependence of the photoionization line shapes on laser pulse energy, it is difficult to form any clear conclusions from these spectra concerning details of the differences introduced by using a different pair of intermediate states. There is no question, however, that the interference using these two states still leads to asymmetric spectra. We are unable to explain the significance of the difference in laser pulse energies for these two similar sets of spectra. In view of the photoelectron angular distributions discussed in Sec. III, it actually would not have been surprising had we seen a larger qualitative difference in the spectra when using these two different intermediate resonances. We plan to explore these effects more in future work.

D. Relative polarization

In these studies we have also examined the effect of laser polarization on the asymmetry of the photoionization spectra and on the potential for control. As remarked earlier, making the two laser polarizations perpendicular to one another allows us to drive $\Delta m_J=\pm 1$ transitions. This still allows for interference, however, since each of the individual noninterfering interactions obeys the same selection rules. If we define the z axis as the direction of polarization of the green laser, then we have $\Delta m_J=0$ for the first step of the two-photon ionization process via the $6s6p$ intermediate resonance, but $\Delta m_J=\pm 1$ for the second. Conversely, the first step of the process resonantly enhanced by the $6s7p$ or $6s8p$ states will be $\Delta m_J=\pm 1$, but Δm_J will be zero for the ionization by the green laser. For both ionization routes, therefore, the total change in the magnetic quantum number m_J is ± 1. This eliminates the excitation of the $^1S_0$ continuum channel, but all others are open.

We have recorded photoionization spectra and branching ratios for the case where the polarizations of the two laser fields are perpendicular to one another for both UV wavelengths, $\lambda_2=307$ nm and $\lambda_2=279$ nm. For $\lambda_2=307$ nm, nearly resonant with the $6s^2\rightarrow 6s7p$ transition, we used pulse energies of 530 μJ at 554 nm and 65 μJ at 307 nm. The atom-beam density is 5.8×10^7 cm^{-3}. A sample spectrum, taken with $\Delta_2=-0.7$ cm^{-1}, is shown in Fig. 12(c). In these photoionization spectra, we note that the peak ionization yield is approximately doubled for the $6s\,^2S_{1/2}$ and $5d\,^2D_{3/2}$ channels, while excitation into the $5d\,^2D_{5/2}$ channel is halved when compared to the photoionization spectra with parallel polarizations. Additionally, these spectra show a stronger asymmetry than we observe for the parallel polarization case. In other words, the asymmetry persists for larger detunings for perpendicular polarizations than for parallel polarizations. It is then surprising that we observe very little control over the branching ratios. This implies that the spectra for the two channels are nearly the same shape, aside from an overall scaling factor.

For $\lambda_2=279$ nm, nearly resonant with the $6s^2\rightarrow 6s8p$ transition, we use pulse energies of 360 μJ (green) and 130 μJ (UV) and the atom-beam density is 5.8×10^7 cm^{-3}. The asymmetry of these spectra, while much less than what we observe for spectra with $\lambda_2=307$ nm, is still much greater than that of the spectra taken with parallel polarizations. For example, compare the spectra in Figs. 12(b) and 12(a). We

also note that the off-resonant line shapes are much narrower than those when the two lasers are polarized parallel to one another. This is not related to the interference effect we are studying since it is still present when only one excitation route is active.

In conclusion, we observe that perpendicular polarization leads to highly asymmetric photoionization spectra, but to very little control over the branching ratio of the products. There is no fundamental reason we know of that more pronounced control of the branching ratio should not be achievable under the crossed polarization condition. Perhaps we have simply not yet achieved the right laser intensities and/or beam density to show this.

VI. CONCLUSION

In this paper we have discussed our observations of the strong interference between two two-photon ionization processes. These effects lead to very asymmetric line shapes for the photoionization spectra and to strong variation of the branching ratios for excitation of the different continuum channels. This interference is independent of the relative phase of the two lasers driving the ionization processes, making the control relatively simple to observe. The interference is insensitive to alignment or careful overlap of the lasers and is therefore very robust. Our studies of the dependence of this interference on the density of the atomic beam show large variation over a relatively narrow range. It is surprising that the dependence of this interference and control on the density of the atoms is so strong. Saturation of the transition by at least one of the laser fields also seems to be important in these control processes. We have shown that the interference is not unique to one pair of two-photon interactions by tuning the frequency of our UV beam from 307 nm to 279 nm, nearly resonant with the $6s^2\,{}^1S_0 \rightarrow 6s8p\,{}^1P_1$ transition. Even though the $6s8p\,{}^1P_1$ couples to the continuum wave functions in different proportions, we are still able to observe effects of the interference. Finally, while we expected that control with parallel or perpendicular polarizations should be possible, for the perpendicular case we have observed only weak control.

There are several outstanding issues surrounding this laser-phase-insensitive control. We have yet to identify the mechanism that leads to an increased capacity for control as the atom density is increased. Similarly, a detailed explanation of the dependence of the control on the relative laser intensities is lacking. It is perhaps premature to attempt any firm conclusions concerning the role of the intermediate states and polarization effects. We intend future investigations expanding our studies of these effects.

ACKNOWLEDGMENTS

This work was supported by the National Science Foundation under Grant No. 9422597-PHY. Technical contributions to this work by M. Rifani through his design and fabrication of the electron mirror are also gratefully acknowledged.

[1] Paul Brumer and Moshe Shapiro, Acc. Chem. Res. **22**, 407 (1989); M. Shapiro, J. W. Hepburn, and P. Brumer, Chem. Phys. Lett. **149**, 451 (1988); C. K. Chan P Brumer, and M. Shapiro, J. Chem. Phys. **94**, 2688 (1992).

[2] Ce Chen, Yi-Yian Yin, and D. S. Elliott, Phys. Rev. Lett. **64**, 507 (1990); Ce Chen and D. S. Elliott, *ibid.* **65**, 1737 (1990).

[3] S. M. Park, S. -P. Lu, and R. J. Gordon, J. Chem. Phys. **94**, 8622 (1992).

[4] G. Xing, X. Wang, X. Huang, R. Bersohn, and B. Katz, J. Chem. Phys. **104**, 826 (1996); X. Wang, R. Bersohn, K. Takahashi, M. Kawasaki, and H. L. Kim, *ibid.* **105**, 2992 (1996).

[5] H. G. Muller, P. H. Bucksbaum, D. W. Schumacher, and A. Zavriyev, J. Phys. B **23**, 2761 (1990); D. W. Schumacher, F. Weihe, H. G. Muller, and P. H. Bucksbaum, Phys. Rev. Lett. **73**, 1344 (1994).

[6] N. B. Baranova, I. M. Beterov, B. Ya. Zel'dovich, I. I. Ryabtsev, A. N. Chudinov, and A. A. Shul'ginov, Pis'ma Zh. Eksp. Teor. Fiz. **55**, 431 (1992) [JETP Lett. **55**, 439 (1992)].

[7] Yi-Yian Yin, Ce Chen, D. S. Elliott, and A. V. Smith, Phys. Rev. Lett. **69**, 2353 (1992); Yi-Yian Yin, D. S. Elliott, R. Shehadeh, and E. R. Grant, Chem. Phys. Lett. **241**, 591 (1995).

[8] B. Sheehy, B. Walker, and L. F. DiMauro, Phys. Rev. Lett. **74**, 4799 (1995).

[9] V. D. Kleinman, L. Zhu, X. Li, and R. J. Gordon, J. Chem. Phys. **102**, 5863 (1995).

[10] E. Dupont, P. B. Corkum, H. C. Liu, M. Buchanan, and Z. R. Wasilewski, Phys. Rev. Lett. **74**, 3596 (1995).

[11] A. Haché, Y. Kostoulas, R. Atanasov, J. L. P. Hughes, J. E. Sipe, and H. M. van Driel, Phys. Rev. Lett. **78**, 306 (1997).

[12] L. Zhu, V. Kleinman, X. Li, S. P. Lu, K. Trentelman, and R. J. Gordon, Science **270**, 77 (1995).

[13] A. Shnitman, I. Sofer, I. Golub, A. Yogev, M. Shapiro, Z. Chen, and P. Brumer, Phys. Rev. Lett. **76**, 2886 (1996).

[14] F. Wang, Ce Chen, and D. S. Elliott, Phys. Rev. Lett. **77**, 2416 (1996).

[15] Ce Chen and D. S. Elliott, Phys. Rev. A **53**, 272 (1996).

[16] S. T. Pratt, J. Chem. Phys. **104**, 5776 (1996).

[17] Z. Chen, P. Brumer, and M. Shapiro, Chem. Phys. Lett. **198**, 498 (1992); J. Chem. Phys. **98**, 6843 (1993).

[18] C. E. Moore, *Atomic Energy Levels*, Natl. Bur. Stand. Ref. Data Ser., Natl. Bur. Stand. (U.S.) Circ. No. 35 (U.S. GPO, Washington, DC, 1971), Vol. III.

[19] R. D. Hudson, V. L. Carter, and P. A. Young, Phys. Rev. A **2**, 643 (1970).

[20] B. Carré, P. d'Oliveira, P. R. Fournier, F. Gounand, and M. Aymar, Phys. Rev. A **42**, 6545 (1990).

[21] J. A. Armstrong, J. J. Wynne, and P. Esherick, J. Opt. Soc. Am. **2**, 211 (1979).

[22] Norman F. Ramsey, *Molecular Beams* (Oxford University Press, Oxford, 1955), Sec. II.2.

[23] J. C. Garreau, Phys. Rev. A **53**, 486 (1996).